ELSEVIER

Available online at www.sciencedirect.com
ScienceDirect

Journal of Structural Biology 160 (2007) 249–262

Journal of
Structural
Biology

www.elsevier.com/locate/yjsbi

Fast, robust, and accurate determination of transmission electron microscopy contrast transfer function

C.O.S. Sorzano [a,b,*], S. Jonic [c], R. Núñez-Ramírez [a], N. Boisset [c], J.M. Carazo [a]

[a] *Unidad de Biocomputación, Centro Nacional de Biotecnología (CSIC), Campus Universidad Autónoma s/n, 28049 Cantoblanco, Madrid, Spain*
[b] *Department of Ingeniería de Sistemas Electrónicos y de Telecomunicación, University of San Pablo-CEU,*
Campus Urb. Montepríncipe s/n, 28668 Boadilla del Monte, Madrid, Spain
[c] *Université Pierre et Marie Curie, CNRS, IMPMC-UMR7590, Université Paris 7, Paris F-75005, France*

Received 29 March 2007; received in revised form 18 August 2007; accepted 22 August 2007
Available online 29 August 2007

Abstract

Transmission electron microscopy, as most imaging devices, introduces optical aberrations that in the case of thin specimens are usually modeled in Fourier space by the so-called contrast transfer function (CTF). Accurate determination of the CTF is crucial for its posterior correction. Furthermore, the CTF estimation must be fast and robust if high-throughput three-dimensional electron microscopy (3DEM) studies are to be carried out. In this paper we present a robust algorithm that fits a theoretical CTF model to the power spectrum density (PSD) measured on a specific micrograph or micrograph area. Our algorithm is capable of estimating the envelope of the CTF which is absolutely needed for the correction of the CTF amplitude changes.

Keywords: Contrast transfer function; Transmission electron microscope; Power spectrum density; Astigmatism

1. Introduction

Structural biology is a key tool to fully understand the function of macromolecular complexes within living cells (Sali et al., 2003). Transmission electron microscopy (TEM) is a very useful device to acquire structural information about these complexes (Frank, 2002; Henderson, 2004; van Heel et al., 2000). However, the electron microscope distorts the structural information by changing amplitudes and phases of recorded electron waves. This is so due to the aberrations that exist in the microscope as in any imaging device, and to the particular nature of the propagation of electron waves. These distortions can be modeled in Fourier space by a multiplication of the Fourier transform of an ideal two-dimensional projection of a three-dimensional object with the microscope transfer function called in the field Contrast Transfer Function (CTF). The reader interested in a physical justification of the multiplication in Fourier space (or the equivalent linear convolution in real space) as well as in the physical model of the CTF is referred to the works of De Rosier (2000), Philippsen et al. (2007), Unwin (1973), Wade (1992), and Zou (1995).

Aware of the need to select good micrographs relying on their CTF behavior, several works proposed a fast sorting of micrographs with visible Thon rings devoid of astigmatism or drift (Gao et al., 2002; Jonic et al., 2007). Astigmatism itself may not be a negative issue if it can be taken into account by CTF correction algorithms. However, astigmatic images are traditionally rejected when using CTF correction procedures that assume only non-astigmatic images such as CTF correction of volumes from defocus series (Penczek et al., 1997).

---

* Corresponding author. Address: Unidad de Biocomputación, Centro Nacional de Biotecnología (CSIC), Campus Universidad Autónoma s/n, 28049 Cantoblanco, Madrid, Spain. Fax:+34 913724049.
E-mail address: coss.eps@ceu.es (C.O.S. Sorzano).

1047-8477/$ - see front matter
doi:10.1016/j.jsb.2007.08.013

The estimation of CTF parameters is usually performed in two steps:

- *Estimation of the power spectrum density*. The power spectrum density (PSD) determines the amount of energy present at each spectral frequency. Considering the CTF as a transfer function of a linear system that takes an input (unknown) image and transforms it into an output (experimentally observed) image, and without taking into account noise, the PSD of the output image is the PSD of the input image multiplied by the square modulus of the CTF. Therefore, the PSD of experimental images is directly related to the CTF. The estimation of the experimental PSD can be done with classical methods such as periodogram averaging (Avila-Sakar et al., 1994; Fernández et al., 1997; Welch, 1967; Zhu et al., 1997) or parametric methods such as AR or ARMA (Fernández et al., 1997; Velázquez-Muriel et al., 2003). Practically speaking, periodogram averaging is a simple and fast method to estimate the PSD, although the estimates are quite noisy (Broersen, 2000). Conversely, parametric methods are more complex and slower to compute, though PSD estimates seem more accurate (Broersen, 2000; Velázquez-Muriel et al., 2003). The CTF estimation procedure presented in this work can work with both kinds of PSD estimates.
- *Estimation of CTF parameters*. Once the PSD has been computed, CTF parameters corresponding to the experimental PSD are estimated. This is usually done by minimizing some measure of dissimilarity between the experimental PSD and a theoretical PSD determined from the CTF parameters. Some works concentrate only on estimation of parameters such as defocus in two principal directions, astigmatism (Mindell and Grigorieff, 2003) or on the contrast amplitude factor (Toyoshima and Unwin, 1988; Toyoshima et al., 1993). This modeling allows the phase correction of experimental images (Frank, 2006). Some other works estimate the amplitude decay either using a Gaussian envelope (specified by a parameter called B-factor) (Huang et al., 2003; Saad et al., 2001; Mallick et al., 2005; Sander et al., 2003) or by fitting parameters of a physical model (Velázquez-Muriel et al., 2003; Zhou et al., 1996; Zhu et al., 1997). Some of the previous works minimize the dissimilarity between the model PSD and the experimental PSD as 1D functions. These 1D functions (or radial profiles) are obtained by rotationally averaging of the 2D experimental PSD (Saad et al., 2001; Zhou et al., 1996; Zhu et al., 1997) or by elliptical averaging (Mallick et al., 2005). A disadvantage of the radial averaging is that the information about astigmatism is lost. Elliptical averaging is not the ideal solution either since it does not take into account anisotropy of background noise, as shown in this paper. Some other works address a fully 2D optimization (Mindell and Grigorieff, 2003; Velázquez-Muriel et al., 2003). The work of Huang et al. (2003) lies somewhere in between a fully 2D optimization and a 1D optimization, since astigmatism is estimated in averaged sectors.

Once the CTF is estimated it can be corrected with any of the available methods: Wiener filtering (Frank and Penczek, 1995; Grigorieff, 1998), combination of differently defocused volumes (Holmes et al., 2003; Penczek et al., 1997), maximum entropy (Skoglund et al., 1996), iterative data refinement (Sorzano et al., 2004a), direct deconvolution in Fourier space (Stark et al., 1997), Chahine's method (Zubelli et al., 2003), etc.

The CTF estimation method proposed in this work differs from previous methods in many ways, although it takes into account many of their best features. It performs a fully 2D estimation and thus overcomes problems associated with radial/elliptical averaging. It estimates a physical model of the decaying envelope instead of a simplified Gaussian decay. It also estimates the local characteristics of the background noise. With respect to our previous publication on CTF estimation, the new method has a modified model of the background (which allows us to make accurate CTF estimations) but the same physical models of CTF and CTF envelope. We allow astigmatism not only in the CTF defoci but also in each term of the background (that is, we allow anisotropic noise). In this paper, we also show that the background is effectively anisotropic, which means that any model based on a radially/elliptically symmetric background is inaccurate. The optimization strategy presented here is completely different from our previous one (Velázquez-Muriel et al., 2003). This new optimization method relies on enhanced PSDs introduced in Jonic et al. (2007). The use of enhanced PSDs makes optimization robust, which is a necessary requirement when a large number of parameters has to be estimated. Furthermore, the present optimization strategy is faster than the one of our previous approach.

The CTF estimation method presented in this work can be applied to a whole micrograph, its local areas, or an individual particle image. Hence, each particle image may have its own CTF model, and we implicitly account for tilted micrographs whose local areas have different defoci values.

We summarize our PSD model in Section 2.1 and describe our fitting of the experimental PSD in Section 2.2. Results obtained with the new algorithm are reported in Section 3. Finally, we discuss the results (Section 4) and conclude (Section 5).

2. Methods

In this section, we first describe the PSD model that is fitted, then we explain the algorithm that has been developed for fitting the PSD parameters.

2.1. PSD model

We assume that the model of image formation in the electron microscope is (Velázquez-Muriel et al., 2003)

$$p_{\mathrm{experimental}}(\mathbf{r}) = h(\mathbf{r})\bigstar(p_{\mathrm{ideal}}(\mathbf{r}) + p_{n_b}(\mathbf{r})) + p_{n_a}(\mathbf{r}), \tag{1}$$

where $\mathbf{r} \in \mathbb{R}^2$ denotes a spatial location, p_{ideal} is the ideal projection of the 3D object being studied, h is the point spread function (PSF) of the microscope, $\bigstar$ denotes the convolution operation, and $p_{n_b}(\mathbf{r})$ and $p_{n_a}(\mathbf{r})$ represent noise terms added before and after the convolution with the PSF. Given this image formation model, the corresponding PSD is

$$\mathrm{PSD}_{\mathrm{experimental}}(\mathbf{R}) = |H(\mathbf{R})|^2(\mathrm{PSD}_{\mathrm{ideal}}(\mathbf{R}) + \mathrm{PSD}_{n_b}(\mathbf{R})) + \mathrm{PSD}_{n_a}(\mathbf{R}), \tag{2}$$

where $\mathbf{R} \in \mathbb{R}^2$ is a given spatial frequency, H is the Fourier transform of the PSF (i.e., the CTF), and PSD_x is the power spectrum density of p_x.

Even if only one object is imaged (as is the case in cellular tomography), we cannot not know p_{ideal} since generally we do not know the 3D structure of the object under study. When imaging multiple copies of the same object (as is the case in single-particle analysis), it is even more difficult to know p_{ideal} since the orientation of particles is unknown beside their unknown 3D structure. Therefore, we assume that $\mathrm{PSD}_{\mathrm{ideal}}(\mathbf{R}) = 0$, which is not so far from the truth since the noise power is much more important than the signal power in a typical electron micrograph. Moreover, we will assume that the noise before the CTF is white, $\mathrm{PSD}_{n_b}(\mathbf{R}) = K^2$. Under these two hypothesis, the model simplifies to

$$\mathrm{PSD}_{\mathrm{theoretical}}(\mathbf{R}) = K^2|H(\mathbf{R})|^2 + \mathrm{PSD}_{n_a}(\mathbf{R}). \tag{3}$$

The structure of this PSD is formed by two terms. The first one is the PSD of the noise colored by the CTF. The second one is the PSD of the noise after CTF and is referred to as "background" PSD. Models for these two terms are described in Sections 2.1.1 and 2.1.2, respectively.

2.1.1. CTF model

The CTF model used in this work is based on the one already used in Velázquez-Muriel et al. (2003). It is briefly reproduced here for convenience. The interested reader is referred to Velázquez-Muriel et al. (2003), Zhou et al. (1996) and references therein for a justification of each term.

A typical microscope has a frequency response approximated by

$$H_{\mathrm{ideal}}(\mathbf{R}) = -(\sin(\chi(\mathbf{R})) + Q(\mathbf{R})\cos(\chi(\mathbf{R}))), \tag{4}$$

where $Q(\mathbf{R})$ is the fraction of electrons being scattered at each frequency (in our model, it is assumed to be constant, Q_0) and

$$\chi(\mathbf{R}) = \pi\lambda\left(|\Delta f(\mathbf{R})||\mathbf{R}|^2 + \frac{1}{2}C_s|\mathbf{R}|^4\lambda^2\right). \tag{5}$$

C_s represents the spherical aberration coefficient, and $\Delta f(\mathbf{R})$ is the defocus vector given by

$$\Delta f(\mathbf{R}) = (\Delta f_{\mathrm{M}}\cos(\angle\mathbf{R} - \theta), \Delta f_{\mathrm{m}}\sin(\angle\mathbf{R} - \theta)). \tag{6}$$

$\angle\mathbf{R}$ is the angle of the 2D frequency $\mathbf{R}$. The defocus vector describes an ellipse with major and minor semi-axes Δf_{M} and Δf_{m}, respectively. The angle of the major semi-axis with respect to the horizontal axis is θ. λ is the electron wavelength which is computed as

$$\lambda = \frac{1.23 \times 10^{-9}}{\sqrt{V + 10^{-6}V^2}}, \tag{7}$$

where V is the acceleration voltage of the microscope.

A real microscope has a frequency response similar to the ideal one except for a damping envelope $E(\mathbf{R})$, which results in a low-pass filtering of the ideally projected 3D object. Thus, the frequency response of a real microscope is

$$H(\mathbf{R}) = E(\mathbf{R})H_{\mathrm{ideal}}(\mathbf{R}). \tag{8}$$

We consider three different effects hindering the maximum achievable resolution: the beam energy spread, the beam coherence, and the sample drift. The three effects combine into a single envelope function as

$$E(\mathbf{R}) = E_{\mathrm{spread}}(\mathbf{R})E_{\mathrm{coherence}}(\mathbf{R})E_{\mathrm{drift}}(\mathbf{R}). \tag{9}$$

The beam energy spread envelope is computed as

$$E_{\mathrm{spread}}(\mathbf{R}) = \exp\left(-\frac{\left(\left(\frac{\pi}{4}C_a\lambda\right)\left(\frac{\Delta V}{V} + 2\frac{\Delta I}{I}\right)\right)^2}{\log(2)}|\mathbf{R}|^4\right), \tag{10}$$

where C_a is the chromatic aberration coefficient, $\frac{\Delta V}{V}$ is the energy spread of the emitted electrons represented as a fraction of the nominal acceleration voltage, and $\frac{\Delta I}{I}$ is the lens current instability expressed as a fraction of the nominal current.

We compute the beam coherence envelope as (Frank, 2006)

$$E_{\mathrm{coherence}}(\mathbf{R}) = \exp\left(-\pi^2\alpha^2\left(C_s\lambda^2|\mathbf{R}|^3 + |\Delta f(\mathbf{R})||\mathbf{R}|\right)^2\right), \tag{11}$$

where α is the semi-angle of aperture.

Finally, assuming the mechanical displacement perpendicular to the focal plane ΔF and the displacement in the focal plane (drift) ΔR, the envelope due to sample shift is modeled as

$$E_{\mathrm{drift}}(\mathbf{R}) = J_0(\pi\Delta F\lambda|\mathbf{R}|^2)\mathrm{sinc}(|\mathbf{R}|\Delta R). \tag{12}$$

The envelope model E can be well approximated by a Gaussian function (an envelope that has been used in other works, Huang et al., 2003; Saad et al., 2001; Mallick et al., 2005; Sander et al., 2003) if $\Delta F = \Delta R = \frac{\Delta V}{V} = \frac{\Delta I}{I} = 0$ and $C_s\lambda^2|\mathbf{R}|^3 \ll \Delta f(\mathbf{R})|\mathbf{R}|$. However, our model is not simplified in this way and keeps all envelope terms modeling the microscope physics.

Summarizing, the parameters required to fully specify the CTF in our model are

$$\left(K, V, C_s, \Delta f_{\mathrm{M}}, \Delta f_{\mathrm{m}}, \theta, Q_0, C_a, \frac{\Delta V}{V}, \frac{\Delta I}{I}, \alpha, \Delta F, \Delta R\right). \tag{13}$$

We assume that V and C_s are fixed for a given microscope and known by the user. The rest of the parameters, 11 in total, will be searched by our algorithm.

2.1.2. Background PSD model

We assume the noise after the CTF to be colored by the film/scanner or CCD frequency response. Physically modeling the corresponding PSD as the output of a linear system, although possible, is out of the scope of this work. Instead, we will model the background PSD as a linear combination of exponential functions. The main behavior of the background PSD depends with $\mathrm{e}^{-\sqrt{|\mathbf{R}|}}$. However, this term has to be corrected at low resolution with a couple of Gaussians, a positive and a negative one. The formal model for the background noise PSD used in this work is

$$\begin{aligned}\mathrm{PSD}_{n_a}(\mathbf{R}) = b + K_s \exp\left(-|\mathbf{s}(\mathbf{R})|\sqrt{|\mathbf{R}|}\right) + K_G \exp \\ \times \left(-|\mathbf{G}(\mathbf{R})|(|\mathbf{R}| - |\mathbf{C}(\mathbf{R})|)^2\right) - K_g \exp \\ \times (-|\mathbf{g}(\mathbf{R})|(|\mathbf{R}| - |\mathbf{c}(\mathbf{R})|)^2),\end{aligned} \tag{14}$$

where

$$\begin{aligned}\mathbf{s}(\mathbf{R}) &= (s_{\mathrm{M}} \cos(\angle\mathbf{R} - \theta_s), s_{\mathrm{m}} \sin(\angle\mathbf{R} - \theta_s)),\\ \mathbf{C}(\mathbf{R}) &= (C_{\mathrm{M}} \cos(\angle\mathbf{R} - \theta_G), C_{\mathrm{m}} \sin(\angle\mathbf{R} - \theta_G)),\\ \mathbf{G}(\mathbf{R}) &= (G_{\mathrm{M}} \cos(\angle\mathbf{R} - \theta_G), G_{\mathrm{m}} \sin(\angle\mathbf{R} - \theta_G)),\\ \mathbf{c}(\mathbf{R}) &= (c_{\mathrm{M}} \cos(\angle\mathbf{R} - \theta_g), c_{\mathrm{m}} \sin(\angle\mathbf{R} - \theta_g)),\\ \mathbf{g}(\mathbf{R}) &= (g_{\mathrm{M}} \cos(\angle\mathbf{R} - \theta_g), g_{\mathrm{m}} \sin(\angle\mathbf{R} - \theta_g)).\end{aligned} \tag{15}$$

The first term provides a constant baseline; the second term is a decaying exponential representating the background PSD behavior; the third and fourth terms of the model are intended to provide more flexibility in the PSD modeling process. The second term will be referred to as the $\sqrt{}$-exponential term because of its dependence on the square root of the frequency. The third and fourth terms will be referred to as the positive and negative Gaussians, respectively. To simplify the writing of equations we will use the following notation for the background PSD

$$\begin{aligned}\mathrm{PSD}_{n_a}(\mathbf{R}) &= b + \mathrm{PSD}_{\sqrt{}}(\mathbf{R}) + \mathrm{PSD}_G(\mathbf{R}) - \mathrm{PSD}_g(\mathbf{R})\\ &= \mathrm{PSD}_{\mathrm{lower}}(\mathbf{R}) - \mathrm{PSD}_g(\mathbf{R}).\end{aligned} \tag{16}$$

All terms are assumed to be elliptically symmetric accounting for a possible anisotropy of the noise after convolution with the CTF. Parametrical models of the corresponding ellipses are given in Eq. (15) and their interpretation is analogous to that of Eq. (6).

Summarizing, there are 17 parameters defining the background PSD, namely

$$(b, K_s, s_{\mathrm{M}}, s_{\mathrm{m}}, \theta_s, K_G, G_{\mathrm{M}}, G_{\mathrm{m}}, C_{\mathrm{M}}, C_{\mathrm{m}}, \theta_G, K_g, g_{\mathrm{M}}, g_{\mathrm{m}}, c_{\mathrm{M}}, c_{\mathrm{m}}, \theta_g). \tag{17}$$

2.2. CTF determination procedure

The experimental PSD must be first estimated from the micrograph image in real space. Periodogram averaging (Avila-Sakar et al., 1994; Frank, 2006; Zhu et al., 1997) is a very popular algorithm to do this due to its simplicity and computational speed. The main drawback of this estimator is that it is very noisy having a standard deviation of the same size as the quantity to be estimated (Broersen, 2000). Alternative estimators are based on parametric models (AR, ARMA) and they have been successfully applied in electron microscopy (Fernández et al., 1997; Velázquez-Muriel et al., 2003). The main disadvantages of these estimators are that they require a large computational time and that they cannot reproduce regions where the PSD is strictly zero.

The CTF determination procedure described below can work with any PSD estimator. In the experiments presented in this work, we only used periodogram averaging since the CTF determination algorithm introduced here is robust enough to tolerate the high amount of noise typical of periodogram averaging. However, in difficult specific cases, parametric models may be used instead to provide much cleaner and more accurate estimations of experimental PSDs.

Our CTF determination algorithm searches automatically for the values of the 28 unknown parameters (11 for the CTF and 17 for the background noise) determining the theoretical PSD that best fits the experimental PSD. This fit is evaluated as a fit of two 2D images. The determined CTF is therefore also a 2D image. That is, CTF astigmatism as well as background noise anisotropy are explicitly taken into account.

Attempting to look simultaneously for all 28 parameters without any guidance is a formidable task for any optimization algorithm. Hence, the optimization problem is divided into smaller subproblems that can be easily solved either because there is an analytical solution or because they involve the adjustment of a few parameters with respect to the values of parameters found in a previous step of the algorithm. Therefore, the parameters of the CTF as well as those of the background PSD are determined in the following four subsequent steps:

- Step 1: Determination of the theoretical PSD lower bound.
- Step 2: Determination of the theoretical PSD upper bound.
- Step 3: Defocus determination.
- Step 4: Final model adjustment.

As will be further explained, the fitting is always done by minimizing a given measure of error between a 2D experimental PSD and a 2D theoretical PSD computed for the values of parameters known at that stage (parameters are progressively estimated; thus, in the first substeps only a few of them are known). In our algorithm, the dissimilarity between two 2D images is usually computed based on the l_1-norm of the error vector. This is so since computing the absolute value of a given quantity is much faster than performing a multiplication (related to the more popular l_2-norm). The employed optimizer is the Powell's conjugate gradient algorithm (Press et al., 1992) which is known for a fast local convergence without the need of explicit derivatives of the goal function. However, there are situations in which the problem structure is simple enough so that a solution of the weighted l_2-norm optimization problem can be analytically computed. In these cases, we first compute the analytical solution of the corresponding weighted l_2-norm optimization problem, and then input it to Powell's algorithm as the initial solution of the l_1-norm related problem.

Except in Step 4c (see below), all optimizations are performed by considering a coarse regular grid of frequencies. That is, we do not compare all possible frequencies since this would result in a much slower algorithm. In the last optimization step, the coarse regular grid is made finer and finer until all available frequencies are used for the fitting.

For the purpose of illustration of the optimization procedure, we performed the estimation of the CTF for an experimental cryo-EM image recorded on a JEOL JEM 2100F electron microscope equipped with a field emission gun. The image was recorded under low dose conditions with a magnification of 50,000×, an acceleration voltage of 200 kV, and a spherical aberration of 0.5 mm, and it was digitized with a pixel size of 1.59 Å × 1.59 Å. In the succeeding sections, we show the computed theoretical PSD for this image after each performed optimization step. This experimental image has been chosen because it is almost non-astigmatic. The radial average can therefore be shown for clarity of illustration. Indeed, although all the optimization is fully performed in 2D, explicitly considering CTF astigmatism and noise anisotropy, we show mainly overlapped radial averages of the experimental and theoretical PSDs. 2D images or particular 1D radial profiles are shown only at the stages were they give more visual information than the radial average.

2.2.1. Step 1: determination of the theoretical PSD lower bound

The estimation of the theoretical PSD lower bound is performed in four substeps:

- *Steps 1a and 1b.* Adjustment of initial values of the $\sqrt{\ }$-exponential parameters and of the baseline.
- *Steps 1c and 1d.* Adjustment of initial values of the positive Gaussian parameters.

2.2.2. Steps 1a and 1b: adjustment of initial values of the $\sqrt{\ }$-exponential parameters and of the baseline

In this step, we compute rough estimates of parameters b, K_s, s_{M}, s_{m}, and θ_s. First, an initial guess with $s_{\mathrm{M}} = s_{\mathrm{m}}$ and $\theta_s = 0$ is found so that the weighted l_2-norm of the error between the experimental PSD and the theoretical PSD is minimized. Second, this solution is refined now letting $s_{\mathrm{M}} \neq s_{\mathrm{m}}$ and $\theta_s \neq 0$ so that it optimizes the error in the l_1 sense. Finally, the theoretical PSD is further refined by optimization of a penalized l_1-error measure. This penalization moves down the estimated $\mathrm{PSD}_{\mathrm{theoretical}}$ so that it becomes a lower bound of the experimental PSD. The radial average of the experimental PSD and the one of the theoretical PSD after Steps 1a and 1b, for the experimental image described in Section 2.2, can be seen in Fig. 1.

1. *Step 1a.* Parameters K_s, s_{M}, s_{m}, and θ_s are sought with the constraints $s_{\mathrm{M}} = s_{\mathrm{m}}$ and $\theta_s = 0$ so that the l_2 norm of the error between the experimental PSD and the theoretical PSD is minimized. This is achieved by the weighted least-squares solution of the equation system
$$\log(\mathrm{PSD}_{\mathrm{experimental}}(\mathbf{R})) = \log(K_s) - s_{\mathrm{M}}\sqrt{|\mathbf{R}|}, \tag{18}$$
where we have one equation for each $\mathbf{R}$ in a regular grid $\Omega \subset \mathbb{R}^2$, the region in the frequency space where the two PSDs (experimental and theoretical) are being compared. In practice, Ω is an annular region defined by the inner and outer radii specified by the user. It is important to judiciously select this region since at very low frequencies the approximation $\mathrm{PSD}_{\mathrm{ideal}}(\mathbf{R}) = 0$ is not valid. The weight of each one of these equations is
$$w(\mathbf{R}) = 1 + \max_{\mathbf{R}' \in \Omega} |\mathbf{R}'| - |\mathbf{R}|, \tag{19}$$
That is, the goal function to be minimized is
$$L = \sum_{\mathbf{R}_i \in \Omega} w(\mathbf{R}_i)\left(\log\left(\mathrm{PSD}_{\mathrm{experimental}}(\mathbf{R}_i)\right) - \log(K_s) + s_{\mathrm{M}}\sqrt{|\mathbf{R}_i|}\right)^2 \tag{20}$$
The weighted least-squares solution of such an equation system can be found in Lawson and Hanson (1995).
2. *Step 1b.* The first guess of the $\sqrt{\ }$-exponential term obtained in the previous step is refined and pushed down in this step. To this goal, the two constraints $s_{\mathrm{M}} = s_{\mathrm{m}}$ and $\theta_s = 0$ are removed, the parameter b (whose initial value is 0) is also estimated, and the error is penalized at frequencies where the theoretical PSD is above the experimental PSD. Thus, the functional to be minimized in this step is
$$L = \sum_{\mathbf{R}_i \in \Omega} \left|\mathrm{PSD}_{\mathrm{experimental}}(\mathbf{R}_i) - \left(b + \mathrm{PSD}_{\sqrt{\ }}(\mathbf{R}_i)\right)\right| \left(1 + W I_{\mathrm{PSD}_{\mathrm{experimental}} < \mathrm{PSD}_{\mathrm{theoretical}}}(\mathbf{R}_i)\right), \tag{21}$$
where $I_A(x)$ denotes the indicator function (this function is 1 if x belongs to the set A, and is 0 otherwise), W is the penalization weight and follows the sequence 0, 2, 4, 8, 16, and 32. For each W, Powell's conjugate gradient algorithm is used to minimize the penalized functional

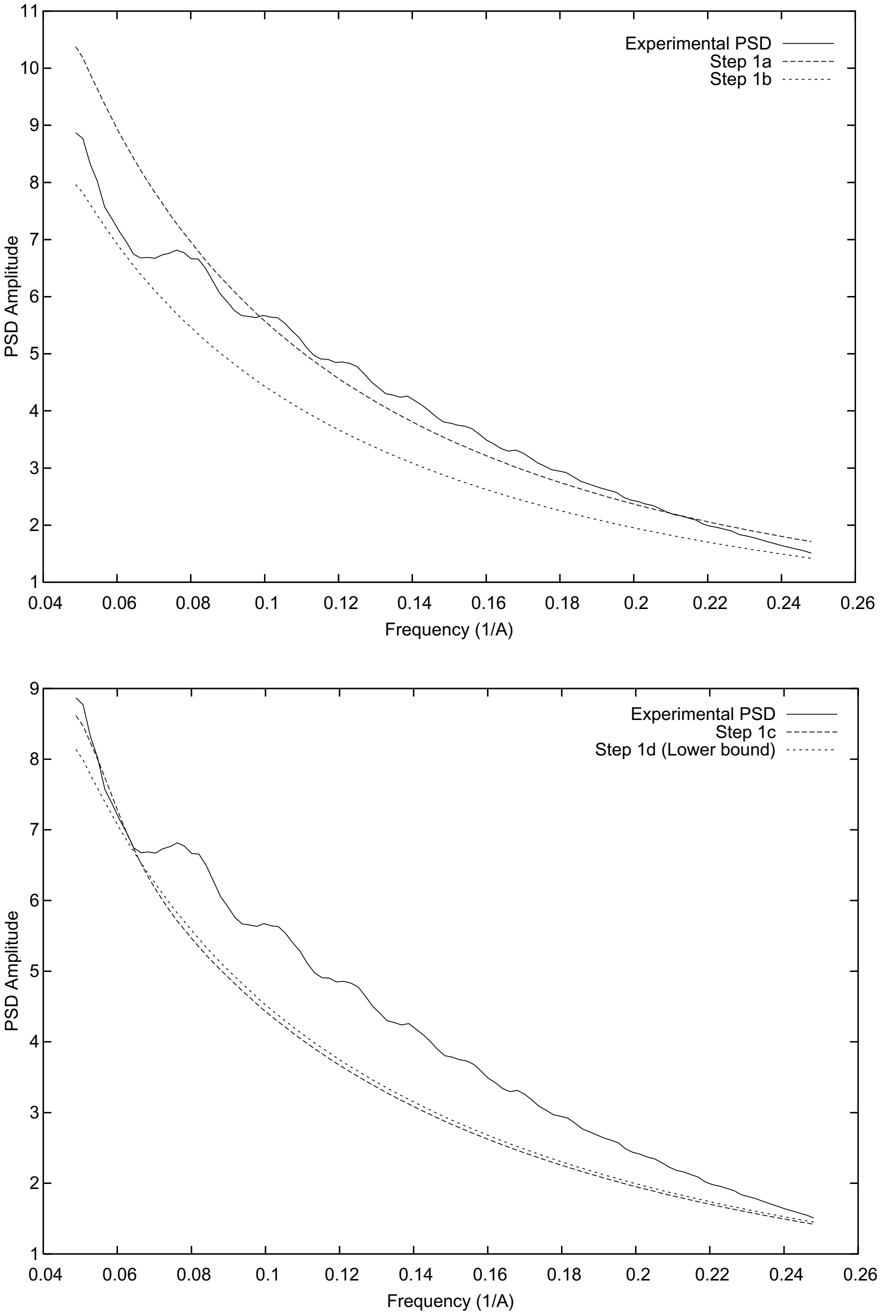

Fig. 1. Radial average of the experimental PSD and the theoretical PSD lower bound after Steps 1a, 1b (top) and 1c, 1d (bottom). After Step 1a, the lower bound goes amid the experimental PSD. In Step 1b, the lower bound is pushed down below the experimental PSD. In Step 1c, we correct the lower bound found in Step 1b by first estimating a radial Gaussian centered at low frequencies. Step 1d defines the theoretical PSD lower bound.

starting from the solution obtained for the previous value of W.

2.2.3. Steps 1c and 1d: adjustment of initial values of the positive Gaussian parameters

In this step, we compute rough estimates of parameters K_G, C_{M}, C_{m}, G_{M}, G_{m}, and θ_G and refine these newly introduced parameters together with the ones of the baseline and the $\sqrt{}$-exponential term (b, K_s, s_{M}, s_{m}, and θ_s). As in Steps 1a and 1b, the positive Gaussian term of the background PSD is computed in two steps: first, a constrained l_2-error optimization is performed on a low frequency region of the experimental PSD previously radially symmetrized. This produces a radially symmetric Gaussian that helps the $\sqrt{}$-exponential term to reproduce the low frequency spectrum of the experimental PSD; second, the condition of radial symmetry of the Gaussian is removed, and a penalized l_1-error optimization is performed. The radial average of the experimental PSD and the one of the theoretical PSD after these two steps, for the experimental image described in Section 2.2, can be seen in Fig. 1.

1. *Step 1c*. The experimental PSD is radially symmetrized as well as the penalized $\sqrt{\ }$-exponential term and baseline found in Step 1. Starting from the lowest frequency, we look for the first frequency at which the two curves are closer. This frequency called $\mathbf{R}_{\min}$ determines the end of the low frequency region. Within this region, we look for the frequency at which the two curves are more separated, $\mathbf{R}_{\max}$. Parameters C_{M} and C_{m} are set to $C_{\mathrm{M}} = C_{\mathrm{m}} = \mathbf{R}_{\max}$. θ_G is set to 0, and G_{M} is constrained to be equal to G_{m}. Therefore, only parameters K_G and G_{M} are left. They are chosen so that they minimize the weighted l_2-norm of the error between the experimental PSD and the theoretical PSD. This is achieved by the weighted least-squares solution of the equation system,

   $$\log\left(\mathrm{PSD}_{\mathrm{experimental}}(\mathbf{R}) - \left(b + \mathrm{PSD}_{\sqrt{\ }}(\mathbf{R})\right)\right) = \log K_G - G_{\mathrm{M}}(|\mathbf{R}| - C_{\mathrm{M}})^2. \tag{22}$$

   We evaluate this equation in the same spectrial grid points as the one of the $\sqrt{\ }$-exponential, and we give the same weight as in Eq. (19).
2. *Step 1d*. this curve is also pushed down so that it really is a background support. The pushing down is done by minimization of

   $$L = \sum_{\mathbf{R}_i \in \Omega} \left|\mathrm{PSD}_{\mathrm{experimental}}(\mathbf{R}_i) - \mathrm{PSD}_{\mathrm{lower}}(\mathbf{R}_i)\right|(1 + WI_{\mathrm{PSD}_{\mathrm{experimental}} < \mathrm{PSD}_{\mathrm{theoretical}}}(\mathbf{R}_i)) \tag{23}$$

   with respect to all parameters estimated so far. The weight W follows the sequence 0, 2, 4, 8, 16, and 32. The output of this Step 1d is called the theoretical PSD lower bound. It is a fully 2D lower bound although for clarity purposes we only represent its radial average in Fig. 1.

2.2.4. Step 2: determination of the theoretical PSD upper bound

In this step, we search for the following parameters of the envelope: K, C_a, $\frac{\Delta V}{V}$, $\frac{\Delta I}{I}$, ΔF, and ΔR. The other two unknown parameters of the envelope (Δf and α) are coupled in the term $E_{\mathrm{coherence}}$. They will be determined in Step 3 when searching for defocus parameters $(\Delta f_{\mathrm{M}}, \Delta f_{\mathrm{m}}, \theta)$ on which this term depends. Therefore, we assume that $\Delta f(\mathbf{R}) = (0,0)$ and $\alpha = 0$ (i.e., $E_{\mathrm{coherence}}(\mathbf{R}) = 1$) at this point. We set $\mathrm{PSD}_{n_a}(\mathbf{R})$ to its lower bound found in Step 1d and we only look for the envelope parameters. As in Step 1d, the search for the upper bound of the PSD is performed by minimizing a penalized goal function. The goal function used in this step is

$$L = \sum_{\mathbf{R}_i \in \Omega} \left|\mathrm{PSD}_{\mathrm{experimental}}(\mathbf{R}_i) - \left(\mathrm{PSD}_{\mathrm{lower}}(\mathbf{R}_i) + K^2E^2(\mathbf{R}_i)\right)\right| (1 + WI_{\mathrm{PSD}_{\mathrm{experimental}} > \mathrm{PSD}_{\mathrm{theoretical}}}(\mathbf{R}_i)). \tag{24}$$

The initial values of the unknown parameters in this optimization step are

$$\left(K, C_a, \frac{\Delta V}{V}, \frac{\Delta I}{I}, \Delta F, \Delta R\right) = \left(1, C_a^{(0)}, 0, 0, 0, 0\right), \tag{25}$$

where $C_a^{(0)}$ is an initial chromatic aberration coefficient that can be supplied by the user (by default, its value is 0). The penalization W follows the sequence 0, 2, 4, 8, 16, and 32.

The output of this step is referred to as the theoretical PSD upper bound. The radial average of the experimental PSD and those of the theoretical PSD lower and upper bounds, for the experimental image described in Section 2.2, can be seen in Fig. 2. The lower and upper bounds will be used in the next two steps to weight the PSD fitting errors.

2.2.5. Step 3: defocus determination

In this step, we determine the defocus parameters $(\Delta f_{\mathrm{M}}, \Delta f_{\mathrm{m}}, \theta)$ and the aperture semi-angle α. First, we compute a rough estimate of the defocus values making use of the estimated lower and upper bounds. Then, we refine all parameters determined until that point.

One of the problems encountered when fitting a PSD model is that the fitting errors committed at high frequencies are of little importance because of the PSD amplitude damping (the PSD amplitude is very small at these high frequencies). Here is where the lower and upper bounds of the PSD come into play to help us define an error measure that is less dependant on the frequency. Given the lower bound $\mathrm{PSD}_{\mathrm{lower}}(\mathbf{R})$ and the upper bound $\mathrm{PSD}_{\mathrm{lower}}(\mathbf{R}) + K^2E^2(\mathbf{R})$, each PSD used in this step is normalized as follows:

$$\widetilde{\mathrm{PSD}}(\mathbf{R}) = \frac{\mathrm{PSD}(\mathbf{R}) - \mathrm{PSD}_{\mathrm{lower}}(\mathbf{R})}{\mathrm{PSD}_{\mathrm{lower}}(\mathbf{R}) + K^2E^2(\mathbf{R}) - \mathrm{PSD}_{\mathrm{lower}}(\mathbf{R})} = \frac{\mathrm{PSD}(\mathbf{R}) - \mathrm{PSD}_{\mathrm{lower}}(\mathbf{R})}{K^2E^2(\mathbf{R})}. \tag{26}$$

This normalization guarantees that any PSD within the lower and upper bounds will be mapped between 0 and 1, and therefore all frequencies will similarly contribute to the PSD fitting error as long as the lower and upper bounds are accurately computed.

The goal function to be minimized at this stage is

$$L = \frac{1}{|\Omega|} \sum_{\mathbf{R}_i \in \Omega} \left|\widetilde{\mathrm{PSD}}_{\mathrm{experimental}}(\mathbf{R}_i) - \widetilde{\mathrm{PSD}}_{\mathrm{defocus}}(\mathbf{R}_i)\right| - \rho\left(\widetilde{\mathrm{PSD}}_{\mathrm{enhanced}}(\mathbf{R}_i), H_{\mathrm{ideal}}(\mathbf{R}_i)E(\mathbf{R}_i)\right), \tag{27}$$

where $|\Omega|$ is the number of spectral grid points in the set Ω, and $\rho(x,y)$ is the correlation coefficient between signals x and y defined as

$$\rho(x,y) = \frac{E\{xy\}}{\sqrt{E\{x^2\}E\{y^2\}}}, \tag{28}$$

where $E\{\cdot\}$ is the expectation operator. $\mathrm{PSD}_{\mathrm{enhanced}}$ is a filtered version of the experimental PSD computed as in Jonic et al. (2007). The experimental PSD and its enhanced version, both used in Step 3 for the image described in Section 2.2, can be seen in Fig. 3. $\mathrm{PSD}_{\mathrm{defocus}}$ is computed as follows:

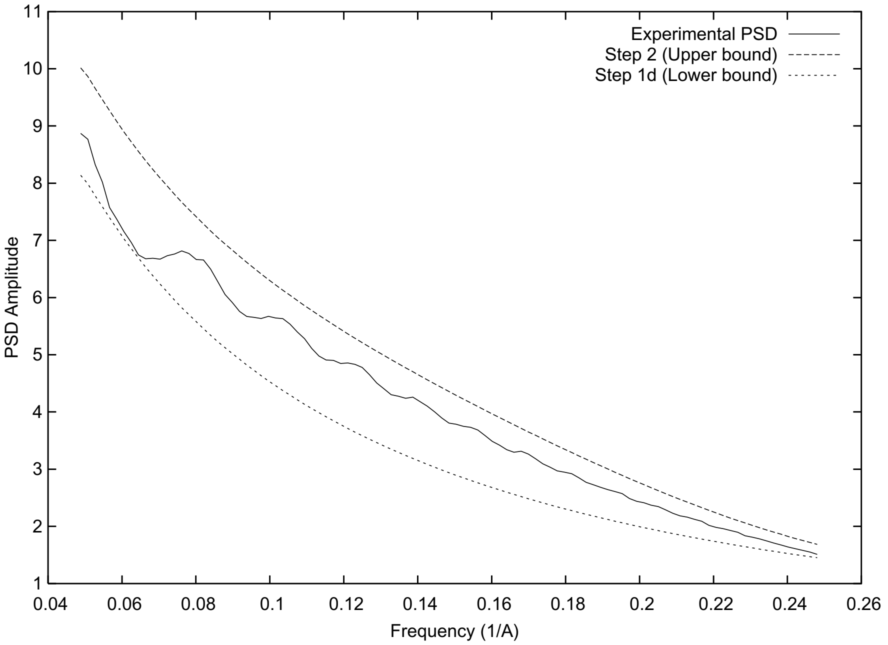

Fig. 2. Radial average of the experimental PSD and the theoretical PSD lower (Step 1d) and upper (Step 2) bounds.

$$\mathrm{PSD}_{\mathrm{defocus}}(\mathbf{R}) = \mathrm{PSD}_{\mathrm{lower}}(\mathbf{R}) + K^2|H(\mathbf{R})|^2. \qquad (29)$$

Again, this step is divided in the following two substeps:

- *Step 3a*. A first estimate of the defocus values is obtained by exhaustive search of the three parameters $(\Delta f_{\mathrm{M}}, \Delta f_{\mathrm{m}}, \theta)$ on a regular grid. Each explored point is used as the initial solution of Powell's conjugate gradient optimizer. This algorithm computes values of the three parameters by minimizing the goal function shown in Eq. (27) and is quite "fast" despite the initial exhaustive search. The best fitting parameters computed at this step are used as the initial solution for Step 3b.
- *Step 3b.* We refine all parameters found so far (23 parameters) by minimizing the goal function in Eq. (27). The only parameters that have not been found yet are those of the negative background Gaussian (PSD_g). They will be determined in Step 4.

The radial average of the experimental PSD, the one of the theoretical PSD after Steps 3a and 3b, as well as those of the theoretical PSD lower and upper bounds, for the experimental image described in Section 2.2, can be seen in Fig. 4.

2.2.6. *Step 4: final model adjustment*

In this step, we estimate first the parameters of PSD_g (Step 4a). Then, we refine all parameters of the model using a coarse grid (the same grid as in all previous steps) (Step 4b). Finally, we refine all parameters using a fine evaluation grid (Step 4c). The output of this step is the output of the CTF determination procedure.

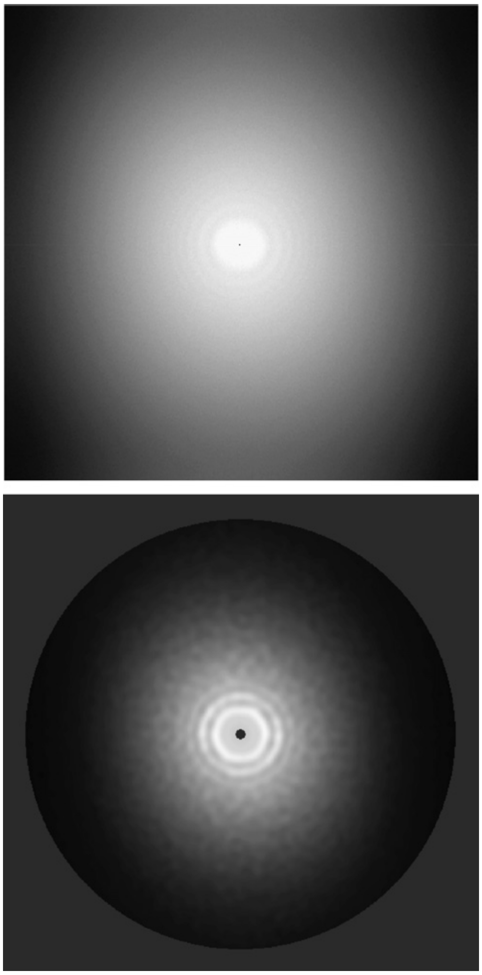

Fig. 3. Experimental PSD (top) and enhanced experimental PSD (bottom).

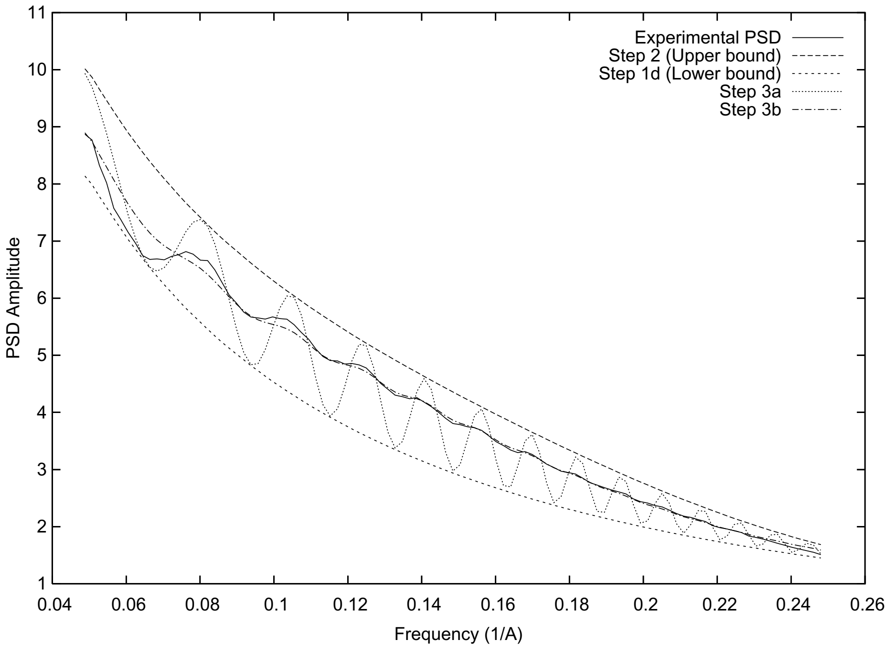

Fig. 4. Radial average of the experimental PSD, the theoretical PSD lower and upper bounds, the theoretical PSD fits after Steps 3a and 3b.

1. *Step 4a*. We compute a first estimate of PSD_g similarly as in Step 1c. We assume the term to be circularly symmetric and therefore $c_{\mathrm{M}} = c_{\mathrm{m}}$, $g_{\mathrm{M}} = g_{\mathrm{m}}$, and $\theta_g = 0$. Thus, this first guess can be found as a weighted least-squares solution of the equation system

   $$\log(\mathrm{PSD}_{\mathrm{lower}}(\mathbf{R}) + K^2|H(\mathbf{R})|^2 - \mathrm{PSD}_{\mathrm{experimental}}(\mathbf{R})) \\ = \log K_g - g_{\mathrm{M}}(|\mathbf{R}| - c_{\mathrm{M}})^2. \qquad (30)$$

   There is one equation for each 2D frequency for which the theoretical PSD estimated in Step 3b is larger than the experimental PSD. We do this because at these frequencies some negative term is needed in order to compensate the difference between the experimental and the theoretical PSDs. Each equation has a weight given by Eq. (19).
2. *Step 4b*. All model parameters are refined on a coarse frequency grid. By default, the coarse grid is defined by taking 1 frequency sample out of 4 consecutive ones in each direction. The goal function to be optimized is shown in Eq. (27).
3. *Step 4c*. The frequency grid is made finer and finer until all available frequencies are used. Thus, the grid is made finer by dividing by 2 the grid spacing until this value is 1. For each grid spacing, the model parameters are refined again using the same goal function and optimization algorithm as in Step 4b.

The radial average of the experimental PSD and the one of the theoretical PSD after Steps 4a, 4b, and 4c for the experimental image described in Section 2.2, can be seen in Fig. 5.

3. Results

Fig. 5 shows that the proposed PSD model correctly reproduces the experimental PSD when using the values of parameters found by the estimation algorithm. However, it is difficult to check the accuracy of the estimated parameters in the case of real micrographs since the true values of parameters are unknown. Moreover, our PSD model is much more complex than the ones used in other programs. Therefore, our estimates cannot be directly compared with the estimates found by other programs. For this reason, we used two different quality assesment setups. In the first setup, simulated micrographs were used to assess the accuracy of the CTF estimation algorithm by measuring the difference between the ground truth PSD and the estimated PSD. In the second setup, experimentally acquired micrographs were used. In this case, we compared the defoci values of our algorithm to those determined by *CTFtilt* (Mindell and Grigorieff, 2003), one of the most widespread programs used to estimate the CTF. In the second setup, we estimated the CTF on two different sets of micrographs: one set from the Large T Antigen (LTag, Gómez-Lorenzo et al., 2003; Valle et al., 2006) and another one from the Glutamate synthase (Glts, Cottevieille et al., in preparation). The two sets have different PSD characteristics.

3.1. Simulated micrographs

Ten micrographs of size 4096 × 4096 pixels with a pixel size of 5.6 Å per pixel were simulated. No particle was present in the simulated micrographs. The CTF parameters used for the simulation were chosen to be the same as one of the micrographs of the LTag micrographs (see below). In this simulated experiment we exactly know the underlying PSD and compared the estimated PSD to the ground truth PSD. The average error of the estimated PSD is $1.2 \pm 0.3\%$ of the true PSD. The error in the smallest

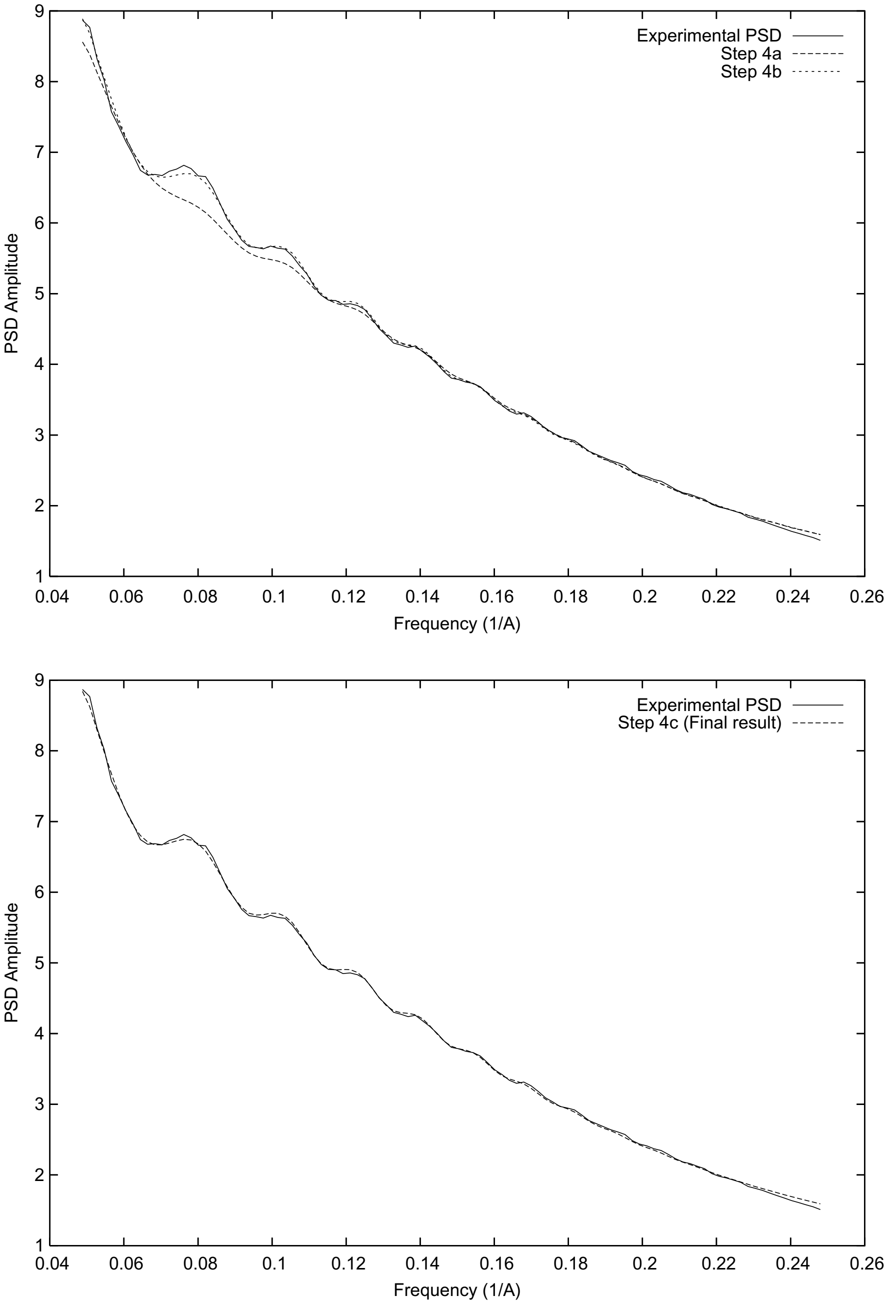

Fig. 5. Radial average of the experimental PSD and the theoretical PSD after Steps 4a, 4b (top) and 4c (bottom).

defocus value was 1.0 ± 0.1%, the error of the largest defocus value was 1.3 ± 0.2%, and the error in the angle of the defocus ellipse was of 2.3 ± 1.8°.

3.2. *Experimental micrographs*

The two sets of experimental images (LTag and GltS) correspond to samples embedded in ice with no carbon. The LTag images had a sampling rate of 5.6 Å per pixel so that the diffraction rings occupy a wide area of the PSD image. The GltS images were digitized with a pixel size of 1.59 Å. Thus, the area occupied by the same number of diffraction rings is smaller in the GltS case than in the LTag case. Fig. 6 shows the (enhanced) experimental PSD and the fitted theoretical PSD for two micrographs, one from each of these groups.

For the search of CTF parameters, we provided our algorithm with the experimental PSD estimated by periodogram averaging, the microscope voltage, the spherical aberration, the micrograph sampling rate, and a wide defocus range for searching (-10^3 Å to -10^5 Å). From both sets of images LTag and GltS, we first removed drifted images as well as images with no visible diffraction rings using sorting of enhanced experimental PSD images as in Jonic et al. (2007). Note that in this step we removed all the images with a strong drift, but that does not mean that

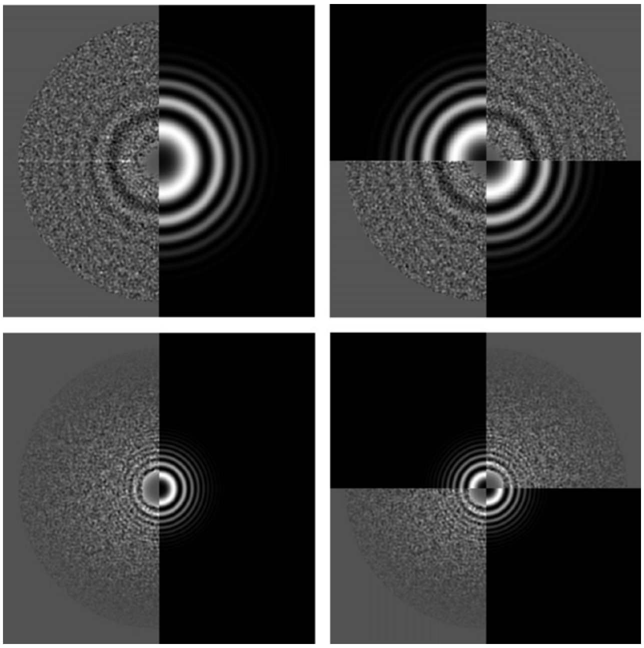

Fig. 6. Top row: CTF model for a LTag micrograph. Bottom row: CTF model for a GltS micrograph. The left image of each row represent the left half-plane of the enhanced PSD, and the right half-plane of the CTF model. The right image makes a similar representation over quadrants. Representing in quadrants have an advantage when trying to visually validate the estimation on astigmatic images.

the drift parameters should not be estimated in the remaining images, since some drift may still be present although it was not so strong as to not consider the image.

The LTag data set contained 92 micrographs of good quality (after the removal of drifted images and images with no visible diffraction rings) taken in a Phillips Tecnai F20 microscope at a magnification of 50,000. The acceleration voltage was 200 kV, and the spherical aberration was 2.26 mm. The defocus range was between −3.5 μm and −7.5 μm. Neither CTFtilt nor the algorithm presented in this paper (from now on, we will refer to it as Xmipp since it is implemented in this software package, Sorzano et al., 2004b) failed to find the CTF parameters. In this context, failure means that the algorithm found defocus values that are clearly not the true ones even if the differences are small one (this can be easily checked by visual inspection). For each micrograph, we considered the ellipse defined by its minor and major defocus values. We compared the minimum defocus provided by CTFtilt and Xmipp. In average, their values in Å differed by 2.7 ± 1.4%. The corresponding maximum defoci differed by 3.5 ± 1.6%. In both cases, the defocus estimated by Xmipp was slightly smaller than the one estimated by CTFtilt (i.e., in the case of minimum defocus, the value estimated by Xmipp was on average a 2.7% smaller than the one of CTFtilt). These differences in defocus values turned into a small difference in the position of the first-zero, on average, the first-zero positions found by the two algorithms differed only by 1.6 ± 0.6%. CTFtilt estimated an average difference between the minimum and maximum defocus values of 1189 ± 734 Å. The same average difference in the case of Xmipp was 770 ± 610 Å.

The GltS data set contained 125 cryo-electron micrographs after the removal of drifted images and images with no visible diffraction rings. They were taken in a JEOL JEM 2100 F microscope at a magnification of 50,000, an acceleration voltage of 200 kV and spherical aberration of 0.5 mm. The defocus range was between −1.7 μm and −3.2 μm. CTFtilt could not find the defoci parameters in 1 occasion, while Xmipp in 3. The parameters returned by the programs in these four occasions were not totally off the true (unknown) parameters, but we could establish visually that the parameters returned were not close enough to the true ones. The hypothesis that both programs have the same failure rate cannot be rejected (confidence of 95%). It should be reminded that Xmipp always provides as part of the solution an estimation of the spectral envelope that CTFtilt does not compute. This piece of information is particularly important for any process related to CTF amplitude correction, as will be further commented in Section 4. The difference between the minimum defocus estimated by CTFtilt and Xmipp was −0.3 ± 1.5% (i.e., Xmipp minimum defocus was slightly larger than the one of CTFtilt), and the corresponding difference for the maximum defocus was 0.4 ± 1.6% (i.e., Xmipp maximum defocus was slightly smaller than the one of CTFtilt). The average difference in the first-zero position between CTFtilt and Xmipp was 0.5 ± 0.4%. The average difference between the minor and major defoci for CTFtilt was 229 ± 163 Å, while it was 404 ± 399 Å for Xmipp.

As has already been shown, our model can estimate astigmatic CTF but also anisotropic background noise. The following example shows that experimental PSDs certainly have anisotropic backgrounds even if the CTF defocus parameters cannot be really considered astigmatic. For the image described in Section 2.2, which is one of the images of the GltS data set, the two defocus parameters as estimated by Xmipp are −22,877 Å and −22,462 Å (the results of the estimation are shown in Figs. 1–5). With a difference of only 415 Å, the corresponding CTF can be considered to be non-astigmatic. However, radial plots along two perpendicular axes show that the two backgrounds are different (see Fig. 7), that is, the background noise level effectively depends on the direction. If the CTF parameters are fitted imposing a radially symmetric background, then the estimated defoci are −21,585 Å and −23,582 Å, i.e., the estimated astigmatism appears to be 1997 Å. This experiment shows that assuming radially symmetric backgrounds may result in inaccurate estimates of the defoci, in this case with an error of about 3.5%.

In order to know whether the anisotropy comes from the microscope or the digitizer we digitized twice the same micrograph with a rotation of 90° between the two scanned images. Fig. 8 shows the final fit performed on the x- and y-axes in the micrograph at 0°, and the plot of the final fit on

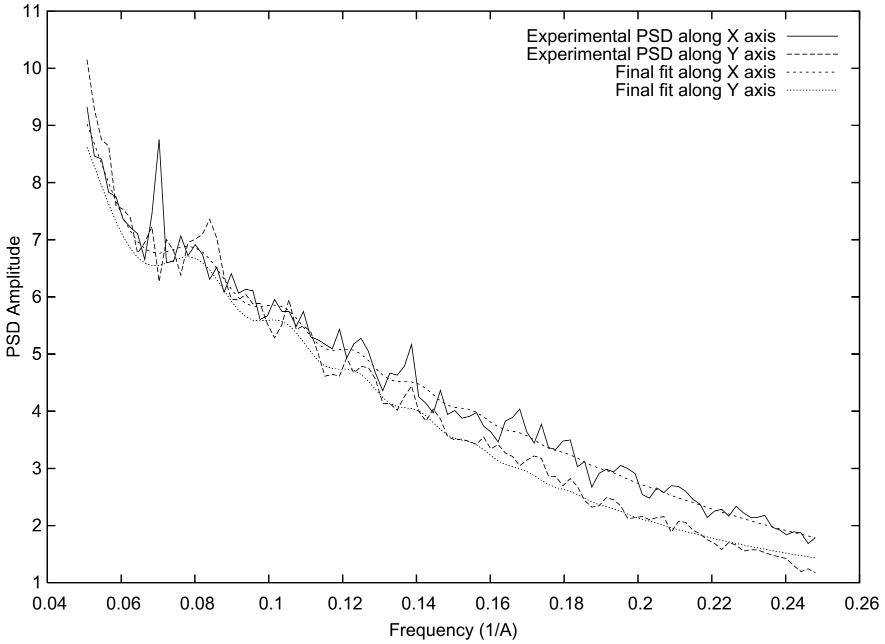

Fig. 7. Radial plots along two perpendicular axes of the experimental PSDs and the corresponding model fits. It can be seen that the experimental PSDs are much noisier than the corresponding radial average for the same micrograph (see Fig. 5). Note that the background noise level differs between the two directions, this effect is specially noticeable at high frequency.

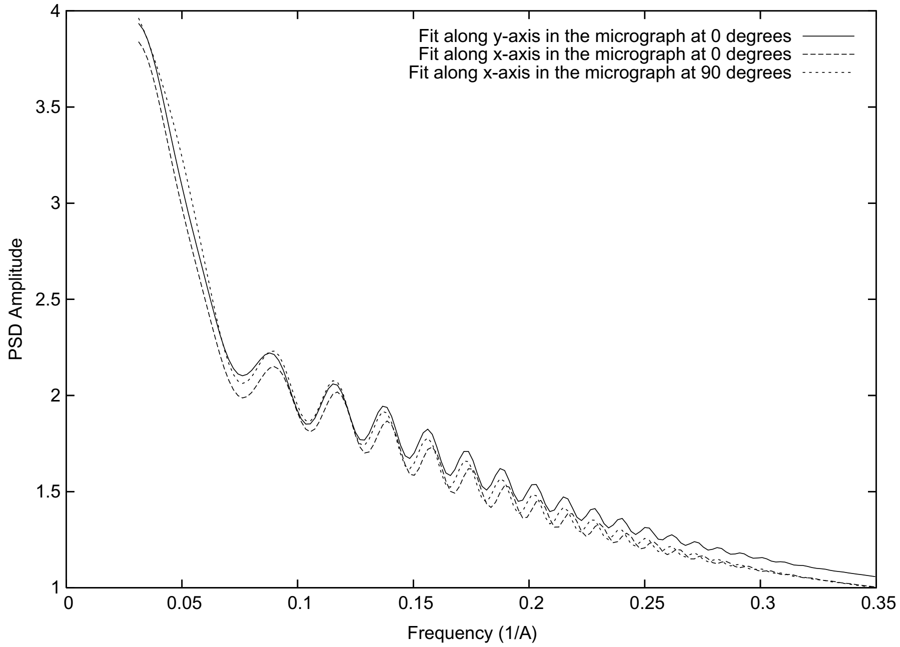

Fig. 8. Plot of the final fit on a micrograph along a given direction, a perpendicular direction in this micrograph, and a direction equivalent to the first plot in the 90° rotated micrograph.

the *y*-axis in the micrograph digitized at 90° (the *x*-axis in the micrograph at 90° corresponds to the *y*-axis in the micrograph at 0°). It can be seen that at low frequency the fits along the two equivalent axes are similar, while at high frequency the fit along the *y*-axis in the micrograph at 90° is similar to the fit along the *y*-axis of the micrograph at 0°. From this fact, it can be concluded that in the experiment carried out anisotropy was due to both devices (electron microscope and digitizer).

4. Discussion

An accurate estimation of the CTF function is crucial for its subsequent correction. If the correction used is only phase-flipping, it suffices to know the values of the defocus parameters. However, if the amplitude decay is also to be corrected, it is very important to accurately determine the CTF envelope. The envelope model used in this paper is justified by the physics of the electron microscope and simplifies to the more popular Gaussian decay used in other works (Huang et al., 2003; Saad et al., 2001; Mallick et al., 2005; Sander et al., 2003). This is one of distinctive features of our algorithm. An additional important feature of our PSD model is the background noise model. It allows for anisotropic noise and makes use of a novel negative Gaussian term which allows a more accurate modeling in the low frequency part of the spectrum (see Figs. 5 and 7). Fig. 7 shows that the use of anisotropic background noise is particularly important for a correct estimation of the amplitude parameters. Anisotropic background noise also suggests that the use of radial averaging of the estimated experimental PSD may mask differences in amplitude decays over different directions. Thus, CTF estimates based on radial averages may be biased. CTF estimates computed on elliptical averages are not safer since the elliptical averaging is usually computed using the CTF astigmatism that, as shown in the example of Fig. 7, may be less important than the anisotropic noise.

To correctly find all parameters of our model, we followed a careful optimization plan that progressively finds the unknown parameters. Background parameters are determined first, then envelope parameters, and finally defocus parameters. The successive optimization steps aim at simplifying the global optimization of CTF and noise parameters and avoiding to get trapped in local minima. However, this is not always possible and the algorithm did not automatically find the CTF parameters in 3 out of 217 micrographs (about 1.4% of the micrographs). It is worth to stress that in 98.6% of the cases, we are providing not only estimates of the zeros of the CTF, but also of the spectral envelope. This additional information is key in recovering the amplitude of the object under study as part of any restoration process, especially at high frequencies. Furthermore, the error rate can be smaller if the user provides a narrower defocus range (the one used in our experiment was from -10^3 Å to -10^5 Å). Robustness of the optimization procedure is greatly improved by the use of enhanced PSDs without which the failure rate increases up to about 30%.

It must be taken into account that our algorithm optimizes the fitting of a theoretical model of the PSD to the experimentally observed PSD. Therefore, all the conclusions can be done at the PSD level (for instance, which is the amplitude of the CTF at a given frequency) but not at the parameter level, i.e., individual parameters (chromatic aberration, energy spread, etc.) cannot be taken as the parameters faithfully representing the physical configuration of the microscope. All that can be said is that the combination of parameters returned by the algorithm faithfully explains the experimental PSD. In fact, some cross-talking between parameters is expected: some envelope decay actually explained at the physical level by a given parameter might be shifted by the algorithm into some other envelope parameter. Although also possible, cross-talking between envelope and background parameters should not be so important.

Thanks to the use of the enhanced PSD, our algorithm is robust enough to work with estimates of the experimental PSD computed by periodogram averaging. Thus, the algorithm described here is a much advanced version of our previous algorithm on CTF estimation (Velázquez-Muriel et al., 2003) in terms of robustness, accuracy and speed. Our current implementation of the algorithm takes only 5 min to estimate the CTF parameters for a PSD estimate of size 512×512 pixels (and the computation of the PSD estimate by periodogram averaging takes only 30 s). These times have been measured on a PC with an Intel Pentium M processor at 1 GHz and 512 Mb of RAM.

Our algorithm fits a PSD theoretical model to an estimate of the experimental PSD. In a more general case of tilted micrographs, our algorithm can be used to divide the micrograph in small areas, to estimate the experimental PSD for each area, and to fit the theoretical model to the estimate of each local experimental PSD. Moreover, if very few particles are to be used from a micrograph, the experimental PSD can be actually estimated for the area that takes into account only the selected particles. In this way, the theoretical PSD model will be as customized as possible to the selected particles.

5. Conclusions

In this paper we have introduced a new algorithm for the determination of the CTF parameters including an accurate estimate of the spectral envelope. The algorithm is fast, accurate, and robust. These three characteristics make it ideal for an automatic image processing workflow in which micrographs are automatically digitized, classified according to the quality of their Thon rings, and for those having good frequency response, the CTF parameters (including the parameters related to the amplitude decay) are automatically estimated. Hence, the proposed algorithm is a new step towards high-throughput electron microscopy. The algorithm is publicly available as a part of the Xmipp software package (http://xmipp.cnb.csic.es).

Acknowledgments

The authors are grateful to Dr. Martn Benito who suggested a new way of showing in the same image the theoretical PSD and the experimental PSD. We acknowledge partial support from the “Comunidad Autnoma de Madrid” through Grant S-GEN-0166-2006, the “Ministerio de Educacin y Ciencia” of Spain through Grants CSD2006-00023, BFU2004-00217, the Spanish FIS Grants PI040683 and 2004-2-OE-192, the European Union through Grants UE-031688, FP6-502828 and the NIH through Grant HL070472.

References

Avila-Sakar, A.J., Guan, T.L., Arad, T., Schmid, M.F., Loke, T.W., Yonath, A., Piefke, J., Franceschi, F., Chiu, W., 1994. Electron cryomicroscopy of bacillus stearothermophilus 50S ribosomal subunits crystallized on phospholipid monolayers. Journal of Molecular Biology 239, 689–697.

Broersen, P.M.T., 2000. Facts and fiction in spectral analysis. IEEE Transactions on Instrumentation and Measurement 49, 766–772.

Cottevieille, M., Jonic, S., Larquet, E., Petoukhov, M.V., Dossena, L., Svergun, D.I., Vanoni, M.A., Boisset, N., in preparation. Structural study of bacterial glutamate synthase complex by 3D cryo-electron microscopy, homology modelling, and small-angle X-ray scattering.

De Rosier, D.J., 2000. Correction of high-resolution data for curvature of the Ewald sphere. Ultramicroscopy 81, 83–98.

Fernández, J.J., Sanjurjo, J., Carazo, J.M., 1997. A spectral estimation approach to contrast transfer function detection in electron microscopy. Ultramicroscopy 68, 267–295.

Frank, J., Penczek, P., 1995. On the correction of the contrast transfer function in biological electron microscopy. Optik 98, 125–129.

Frank, J., 2002. Single-particle imaging of macromolecules by cryo-electron microscopy. Annual Review of Biophysics and Biomolecular Structure 31, 303–319.

Frank, J., 2006. Three-Dimensional Electron Microscopy of Macromolecular Assemblies: Visualization of Biological Molecules in their Native State. Oxford University Press, USA.

Gao, H., Spahn, C., Grassucci, R., Frank, J., 2002. An assay for local quality in cryo-electro micrographs of single particles. Ultramicroscopy 93, 169–178.

Gómez-Lorenzo, M., Valle, M., Frank, J., Gruss, C., Sorzano, C.O.S., Chen, X.S., Donate, L.E., Carazo, J.M., 2003. Large T antigen on the simian virus 40 origin of replication: a 3D snapshot prior to DNA replication. EMBO Journal 22, 6205–6213.

Grigorieff, N., 1998. Three-dimensional structure of bovine NADH: ubiquinone oxidoreductase (complex I) at 22 Å in ice. Journal of Molecular Biology 277, 1033–1046.

Henderson, R., 2004. Realizing the potential of electron cryo-microscopy. Quarterly Review of Biophysics 37, 3–13.

Holmes, K.C., Angert, I.J.K.F., Jahn, W., Schroeder, R.R., 2003. Electron cryo-microscopy shows how strong binding of myosin to actin releases nucleotide. Nature 425, 423–427.

Huang, Z., Baldwin, P.R., Mullapudi, S., Penczek, P.A., 2003. Automated determination of parameters describing power spectra of micrograph images in electron microscopy. Journal of Structural Biology 144, 79–94.

Jonic, S., Sorzano, C.O.S., Cottevieille, M., Larquet, E., Boisset, N., 2007. A novel method for improvement of visualization of power spectra for sorting cryo-electron micrographs and their local areas. Journal of Structural Biology 157, 156–167.

Lawson, C.L., Hanson, R., 1995. Solving least-squares problems. SIAM, Philadephia, PA., USA.

Mallick, S.P., Carragher, B., Potter, C.S., Kriegman, D.J., 2005. ACE: automated CTF estimation. Ultramicroscopy 104, 8–29.

Mindell, J.A., Grigorieff, N., 2003. Accurate determination of local defocus and specimen tilt in electron microscopy. Journal of Structural Biology 142, 334–347.

Penczek, P.A., Zhu, J., Schröder, R., Frank, J., 1997. Three dimensional reconstruction with contrast transfer compensation from defocus series. Scanning Microscopy 11, 147–154.

Philippsen, A., Engel, H.A., Engel, A., 2007. The contrast-imaging function for tilted specimens. Ultramicroscopy 107, 202–212.

Press, W., Teukolsky, S.A., Vetterling, W.T., Flannery, B.P., 1992. Numerical recipes in C, second ed. Cambridge University Press, Cambridge.

Saad, A., Ludtke, S., Jakana, J., Rixon, F., Tsuruta, H., Chiu, W., 2001. Fourier amplitude decay of electron cryomicroscopic images of single particles and effects on structure determination. Journal of Structural Biology 133, 32–42.

Sali, A., Glaeser, R., Earnest, T., Baumeister, W., 2003. From words to literature in structural proteomics. Nature 422, 216–225.

Sander, B., Golas, M.M., Stark, H., 2003. Automatic CTF correction for single particles based upon multivariate statistical analysis of individual power spectra. Journal of Structural Biology 142, 392–401.

Skoglund, U., Ofverstedt, L.G., Burnett, R., Bricogne, G., 1996. Maximum-entropy three-dimensional reconstruction with deconvolution of the contrast transfer function: a test application with adenovirus. Journal of Structural Biology 117, 173–188.

Sorzano, C.O.S., Marabini, R., Herman, G.T., Censor, Y., Carazo, J.M., 2004a. Transfer function restoration in 3D electron microscopy via iterative data refinement. Physics in Medicine and Biology 49, 509–522.

Sorzano, C.O.S., Marabini, R., Velázquez-Muriel, J., Bilbao-Castro, J.R., Scheres, S.H.W., Carazo, J.M., Pascual-Montano, A., 2004b. XMIPP: a new generation of an open-source image processing package for electron microscopy. Journal of Structural Biology 148, 194–204.

Stark, H., Orlova, E.V., Rinke-Appel, J., Junke, N., Müller, F., Rodnina, M., Wintermeyer, W., Brimacombe, R., van Heel, M., 1997. Arrangement of tRNAs in pre- and posttranslocational ribosomes revealed by electron cryomicroscopy. Cell 88, 19–29.

Toyoshima, C., Unwin, N.T.P., 1988. Contrast transfer for frozen-hydrated specimens: determination from pairs of defocused images. Ultramicroscopy 25, 279–292.

Toyoshima, C., Yonekura, K., Sasabe, H., 1993. Contrast transfer for frozen-hydrated specimens II: amplitude contrast at very low frequencies. Ultramicroscopy 48, 165–176.

Unwin, P., 1973. Phase contrast electron microscopy of biological materials. Journal of Microscopy 98, 299–312.

Valle, M., Chen, X.S., Donate, L.E., Fanning, E., Carazo, J.M., 2006. Structural basis for the cooperative assembly of large T antigen on the origin of replication. Journal of Molecular Biology 357, 1295–1305.

van Heel, M., Gowen, B., Matadeen, R., 2000. Single-particle electron cryo-microscopy: towards atomic resolution. Quarterly Review of Biophysics 33, 307–369.

Velázquez-Muriel, J.A., Sorzano, C.O.S., Fernández, J.J., Carazo, J.M., 2003. A method for estimating the CTF in electron microscopy based on ARMA models and parameter adjusting. Ultramicroscopy 96, 17–35.

Wade, R., 1992. A brief look at imaging and contrast transfer. Ultramicroscopy 46, 145–156.

Welch, P.D., 1967. The use of fast Fourier transform for the estimation of power spectra: a method based on time averaging over short, modified periodograms. IEEE Transactions on Audio Electroacoustics AU-15, 70–73.

Zhou, Z.H., Hardt, S., Wang, B., Sherman, M.B., Jakana, J., Chiu, W., 1996. CTF determination of images of ice-embedded single particles using a graphics interface. Journal of Structural Biology 116, 216–222.

Zhu, J., Penczek, P.A., Schröder, R., Frank, J., 1997. Three-dimensional reconstruction with contrast transfer function correction from energy-filtered cryoelectron micrographs: procedure and application to the 70S *Escherichia coli* ribosome. Journal of Structural Biology 118, 197–219.

Zou, X., 1995. Electron crystallography of inorganic structures—theory and practice. Ph.D. thesis, Stockholm University.

Zubelli, J.P., Marabini, R., Sorzano, C.O.S., Herman, G.T., 2003. Three-dimensional reconstruction by Chahine's method from electron microscopic projections corrupted by instrumental aberrations. Inverse Problems 19, 933–949.